ICEF2018-9687

DESIGN AND EXPERIMENTAL VALIDATION OF A SPATIALLY DISCRETIZED, CONTROL-ORIENTED TEMPERATURE MODEL FOR A CERIA-WASHCOATED GASOLINE PARTICULATE FILTER

Sean Moser
Clemson University
Greenville, SC, USA

Simona Onori
Stanford University
Stanford, CA, USA

Mark Hoffman
Auburn University
Auburn, AL, USA

ABSTRACT

Gasoline particulate filters (GPFs) are the most promising and practically applicable devices to reduce Particulate Matter (PM) and Particulate Number (PN) emissions from gasoline direct ignition engines. A model that can predict internal GPF temperature dynamics during regeneration events can then be implemented online to maintain GPF health and aide in exotherm control algorithms without the associated instrumentation costs. This work demonstrates a control-oriented model, which captures the thermal dynamics in a catalyzed, ceria-coated GPF in the axial direction. The model utilizes soot oxidation reaction kinetics to predict internal GPF temperature dynamics during regeneration events using three finite volume cells.

A model methodology initially proposed by Arunachalam et al [18] is utilized with the GPF of this work, validating the broad applicability of that methodology. Then, the model's temperature prediction fidelity is improved through axial discretization. The zonal model parameters are identified via a Particle Swarm Optimization using experimental results from the instrumented GPF. Identified parameters from the various data sets are used to develop a linear parameter varying model for prediction of the axial temperature distribution within the GPF. The resulting model is then validated against an experimental data set utilizing the exhaust temperature entering the GPF. The spatial discretization methodology employed both enables the prediction of spatial temperature variation within the GPF and

improves the accuracy of the peak temperature prediction by a factor ranging from 2-10x.

INTRODUCTION

Gasoline Direct Injection (GDI) engines are gaining appeal with automotive manufacturers as a replacement for Port Fuel Injection Engines [1,8]. The GDI engine benefits from high fuel efficiency (3-6% improvement over port fuel injection [1]) and high power output, resultant from precise control of injected fuel and its timing. Although GDI engines reduce CO_2 emissions, they also produce particulate matter, an unfortunate side effect of fuel stratification, wall wetting, and reduced time available for charge formation. Chan T., et al. [1] found that a GDI engine produced 10 and 31 times higher particulate emissions compared to a port fuel injected (PFI) engine for the FTP-75 and US06 cycles, respectively. Particulate matter (PM) can be reduced by using Gasoline Particulate Filters (GPFs), which are akin to diesel particulate filters. Chan T., et al [1] determined that equipping a GDI engine with a GPF, reduced particulate production to only two and eight times more than a PFI engine for FTP-75 and US06 drive cycles, respectively. Similar research works have shown the effectiveness of GPF utilization for particulate emissions reduction under different driving scenarios [2-6].

GPF implementation is fast becoming a necessity to enable compliance with increasingly stringent PM and particulate number (PN) standards, specifically the Euro 6c PN emission regulations ($< 6 \times 10^{11}$ particles/km). Demuynck et al [4] found

that GDI vehicles without a GPF were close to or exceeding the Euro 6c PN limit. When the same vehicle was equipped with a GPF, the PN emissions were halved for both the New European Driving Cycle (NEDC) and Worldwide Harmonized Light Duty Test Procedure (WLTP) with no net effects on fuel economy [4].

Oxidation of trapped particulates critically depends on both the presence of oxygen and adequate temperature. Unlike diesel particulate filters (DPFs), which operate in lean exhaust streams of relatively low temperature, GPFs are operated in stoichiometric conditions and at higher exhaust temperatures. Thus, the availability of oxygen becomes the limiting factor for GPF regeneration, especially for GPFs located downstream of a three-way catalyst (TWC). Some groups utilize ceria based washcoats doped with catalytic materials to both store oxygen and bolster reactivity. Richter, J. et al. [8] and Xia, W. [9], both showed that a GPF coated with a catalytic material improved soot regeneration, especially for vehicle's operating in urban driving conditions, where exhaust temperature rarely obtains adequate magnitude to initiate passive regeneration. The authors in [8] also investigated different three-way catalyst (TWC) and GPF configurations to analyze the after-treatment system as a whole. A close-coupled TWC and GPF with optimized catalytic coatings further reduced NOx emissions with no effect on fuel consumption. Xia et al [9] also noted that the pressure drop created by a coated GPF was higher than an uncoated GPF, yet no loss in fuel economy was observed over drive cycles. Additionally, with optimized precious metal coating and substrate selection, the TWC can be replaced with a coated GPF without affecting emission reduction capability [9].

In addition to the disparity in operational environments experienced by DPFs and GPFs, the particulate size and exhaust gas properties of GDI differ substantially from diesel [18]. By necessity, the physical GPF design parameters (pore size, total porosity, channel dimensions, wall thickness) must differ from DPFs due to the discrepancies in particulate size and the differing sensitivities of the respective engines to backpressure. There is a significant body of literature focusing on experimental characterization and numerical modeling of DPF operation, yet due to the disparities in operational environments and the utilization of catalyzed washcoats in GPF applications, traditional DPF soot oxidation models are found to be neither physically representative nor transferable to the GPF application.

Accurate physical modeling of the GPF is critical for device health and efficiency control strategies. Modeling of the thermal dynamics during GPF operation is necessary for developing control strategies for GPF lifecycle management. Runaway exothermic reactions can damage the GPF washcoat and/or substrate, rendering the GPF ineffective. Furthermore, management of soot accumulation is required to maintain backpressure at a healthy level, as increased backpressure negatively impacts engine efficiency. Van Nieuwstadt et al. [16], proposed three required control strategies to effectively manage a GPF. One control model is needed to estimate soot accumulation, and the work proposed using an empirical open loop model based on coolant temperature and engine PM maps. A second control method was proposed to heat the GPF for thermally challenged drive cycles. Van Nieuwstadt utilized spark retard (increase in exhaust enthalpy) to elevate GPF temperature and initiate passive soot regeneration. The final proposed control strategy was an exothermic reaction simulation model to ensure the internal GPF temperature does not exceed the material limits of the substrate during a passive regeneration event.

Arunachalam et al. [18] proposed a lumped parameter model to characterize the thermal dynamics in a ceria-coated GPF during regeneration. In the present work, "Lumped Model", "0D", and "Single Zone Model" are used synonymously to describe a model developed equivalently to [18]. The current work improves the estimation of peak temperature rise inside the catalytically washcoated GPF during a regeneration event by expanding the modeling methodology to include spatial discretization. The newly formulated spatial model increases temperature prediction accuracy while retaining enough computationally efficiency to enable online utilization for GPF health management.

This work is organized as follows. First, the experimental instrumentation and methodology utilized for GPF characterization and regeneration data collection are briefly outlined. Then, the GPF modeling methodology is introduced. The existing lumped GPF modeling methodology is then applied to the GPF of this work, including both identification and validation. Then, the spatially discretized GPF modeling methodology is overviewed, and the resulting model is both identified and validated with experimental results. Finally, the performance of the lumped and spatially discretized models are compared and discussed. The work then closes with conclusions.

Experimental Instrumentation

Experiments were conducted on a production vehicle with a 2.0L 4-cylinder turbocharged GDI engine via a chassis dynamometer. The vehicle was equipped with a close-coupled three-way catalyst (TWC), and a washcoated GPF was installed in a subfloor location downstream of the TWC. AVL's IndiCom software was used to record temperature, pressure, lambda, and engine crank based signals (engine load, spark timing, injection timing, and fuel flow measurement). In addition, HP Tuner, an after-market tuning software, was used to record data from the engine control unit (ECU). HP tuner's editor also provided access to spark timing and injection timing maps, which were subsequently modified to facilitate expedient GPF soot accumulation.

Oxygen concentrations are measured using wide band lambda sensors. Pre and post TWC lambda sensors are used to monitor engine operation whereas lambda sensors located both upstream and downstream of the GPF reveal soot burning during regeneration (soot-oxidation) events. Pre and post GPF gaseous
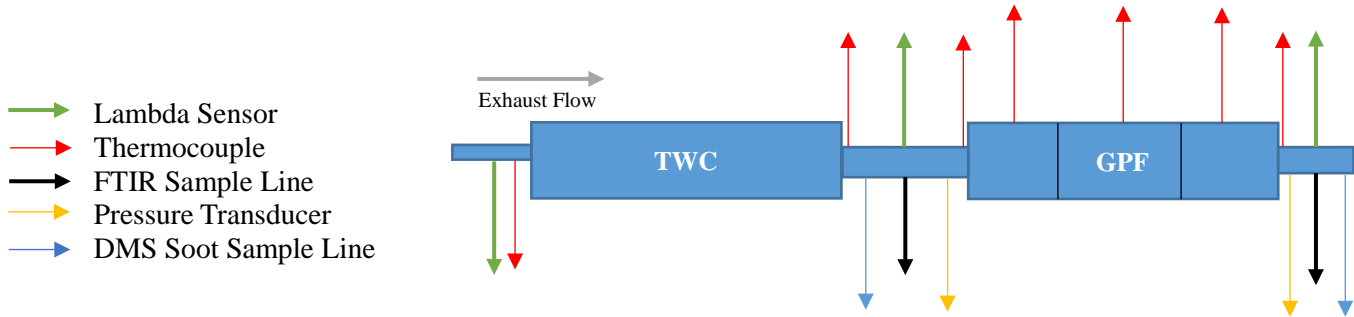
Figure 1: Experimental Set up – Close coupled underfloor TWC and GPF

emissions quantification is simultaneously conducted with a dual-channel AVL i60 Fourier-transform infrared spectroscope (FTIR). Relative differences between critical species (such as CO and CO_2) are then utilized to identify any chemical reactions occurring in the GPF. Soot measurements are sequentially collected pre and post GPF using a Cambustion DMS500 differential mobility spectrometer for real time measurement of particulate size distributions, number, and mass. Differential comparison of pre and post GPF particulate quantification reveals GPF filtering efficiency during soot accumulation.

For accumulation testing, AVL's Micro Soot Sensor (based on the photoacoustic measurement method) was used to measure soot at post GPF location simultaneous with the Cambustion DMS500 at the pre-GPF location, effectively monitoring particulate breakthrough. During the accumulation test, pressure drop across GPF is measured using a differential pressure transducer.

To investigate spatial GPF temperature variations during accumulation and regeneration events, thermocouples were installed in three separate planes orthogonal to the central axis of the GPF as shown in Figure 2. The authors note that the peak temperatures were found in the third plane, furthest from the inlet of the GPF. Peak temperature in this paper refers to the temperatures experimentally found in plane 3. Higher temperatures should exist closer to the outlet of the GPF, but the available experimental data was unable to quantify this theory.
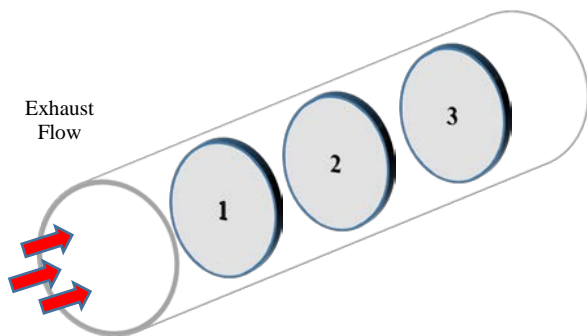

Figure 2: Thermocouple planes along GPF Central Axis

Figure 2 shows the three measurement planes where thermocouples are located, the front plane (1) is 38 mm from the front face, the mid plane (2) is at the center of the GPF, and rear plane (3) is 38 mm from the rear face of the substrate. The GPF ceramic substrate is 110 mm long, and as such, the planes are not evenly spaced.

Experimental Methodology

Three dedicated experiments were conducted on the GPF for thermal model identification and validation . First, to determine the thermal inertia of the GPF, a 'Clean Thermal Sweep' was conducted. The test subjects the GPF to various step changes in inlet gas temperature and waits for the internal temperature of the GPF to stabilize. Second, rapid soot accumulation was required to develop real world soot loading within the GPF. HP Tuner was utilized to modify the spark timing map, and a predetermined speed, load, and spark timing were used to rapidly accumulate soot. Third, regeneration experiments (fuel-cut throttle tip-outs) were conducted to track the temperature within the GPF during soot oxidation. The experiments were conducted in the following order: Clean Thermal Sweep (no soot), soot accumulation (light soot loading), three regeneration fuel cuts, soot accumulation (medium soot loading), five regeneration fuel cuts, soot accumulation (heavy soot loading), five regeneration fuel cuts. Further information on the experimental process, soot accumulation, and instrumentation can be found in Rathod et al [19].

The initiation and completion of the chemical reactions that oxidize carbon stored in the GPF into CO and CO_2 is termed *Regeneration* in this paper. To initiate a regeneration event, high temperature and excess oxygen are required. A high load condition was established on the chassis dynamometer to increase the GPF temperature , and then a throttle tip-out (foot off the pedal) initiated a fuel cutoff, creating lean conditions (oxygen rich, fuel lean) within the GPF. Multiple regeneration events were performed at successively higher tip-out temperatures to oxidize all the accumulated soot within the GPF. These successive tip-outs were analyzed to identify relationships between soot loading and inlet temperature and exothermic internal GPF temperature rise. To maintain the health of both the precious metal laden ceria washcoat and the GPF cordierite

substrate, the maximum temperature limit during regeneration that could be attained momentarily was 1175°K.

Experimental GPF Regeneration Events

The following tip-out experiments were conducted using the test procedure laid out in Rathod et al [19]. The identification data used to develop the linear parameter varying model for both the lumped and spatially discretized models is comprised of eight regeneration fuel cut events. An additional five regeneration fuel cut events are used for model validation. SLD represents the Soot Loading Density, or the amount of soot accumulated in the GPF, normalized by the GPF volume. The temperature of the GPF at time of tip out is indicated and used later for validation.

Table 1: Experimental Data for Model Identification

Data Set	SLD [g/L]	Regen Event	Temperature @ Tip-out [K]	Soot Oxidized [g]
1	0.79	1A	1025	0.46
		1B	1050	0.30
		1C	1075	0.33
2	1.92	2A	975	0.30
		2B	975	0.21
		2C	1050	0.32
		2D	1050	0.29
		2E	1075	0.37

Table 2: Validation Experimental Data

Data Set	SLD [g/L]	Regen Event	Temperature @ Tip-out [K]	Soot Oxidized [g]
3	1.80	3A	975	0.21
		3B	975	0.31
		3C	1050	0.34
		3D	1050	0.15
		3E	1075	0.49

GPF Characterization

The lumped parameter model developed by Arunachalam et al [18] is geometrically representative of a GPF with different physical parameters than the GPF utilized for this investigation. Thus, the volume and specific heat of the current GPF must be identified. As exhaust gas must flow through the porous GPF substrate, a lumped specific heat of the substrate and washcoat was identified using the method developed in Arunachalam et al [18], and Rathod et al [19]. This lumped equivalent specific heat is generalized and referred to as the specific heat of the GPF throughout. Further information on the identification process is laid out in the Model Parameter Identification section.

Table 3: Physical Disparities between the Current GPF and Device Used in [18]

	GPF in [18]	Current GPF
Diameter	118 mm	105 mm
Length	127 mm	110 mm
Specific Heat	1173 J/kg*K	1136 J/kg*K
# of Channels	5085	4081
Volume Cordierite	1.39 L	0.97 L
Trapping Volume	1.22 L	0.84 L

Experimental Data Preparation for Parameter Identification

Due to the compound effects of: exhaust flow mass transport delay, slow (relatively) lambda sensor temporal response, and thermocouple axial conduction; the experimental data traces must all be temporally aligned with the start of the tip out event. This procedure is outlined in detail in [18], but will be quickly overviewed here for completeness.

The Mass Flow Rate trace is matched to the air-fuel ratio atmospheric saturation event. The delay between the mass flow rate and lambda response is associated with the physical transport delay between the two sensors. Mass flow rate is determined from the engine ECU and an intake manifold sensor reading. In contrast, lambda is measured directly before the GPF and downstream of the TWC as shown in Figure 1. This phase delay can be seen in Figure 3.

Additionally, both pre and post GPF CO_2 readings are then shifted together to match the beginning of the tip-out event, defined by the air fuel ratio reaching atmospheric saturation (deceleration fuel shut off event, DFSO). This shift accounts for the equivalent transport delays between the respective measurement locations and the parallel FTIR analyzers, as shown in Figure 4.
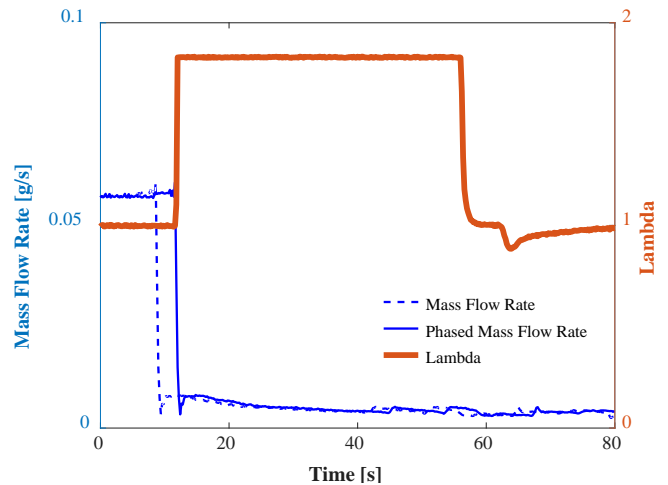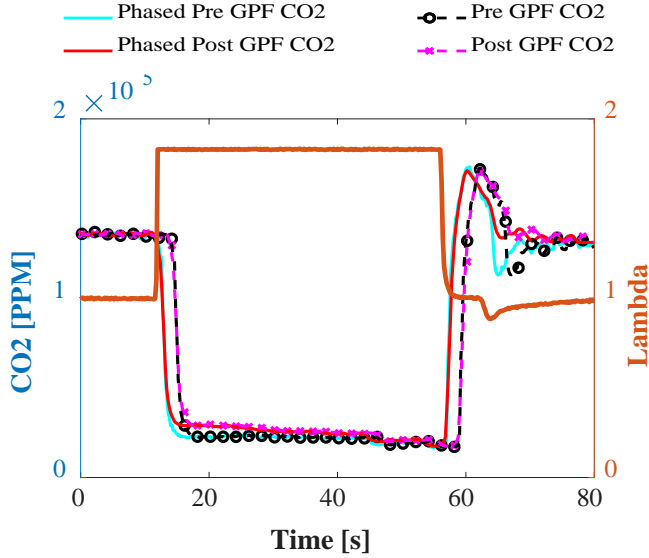

Figure 3: Mass Transfer Delay

Figure 4: Phase Matched Mass Flow Rate and Lambda Signal

GPF Modeling Methodology

A 0-D lumped model was developed by Arunachalam et al [18], which simulated GPF soot oxidation and an average internal GPF temperature. While this model accurately represented the soot oxidation within the GPF and provided an estimate of internal GPF temperature, the lumped average temperature could not capture the peak temperatures within the GPF due to a lack of spatial information. This work expands upon the aforementioned model by (i) validating transference of the modeling technique to a physically different ceria washcoated GPF, and (ii) enhancing the temperature prediction capabilities of the model by spatially discretizing the GPF into three zones. The additional accuracy of the spatial model characterizes the peak temperatures within the GPF, a requisite for a monitoring the health of the GPF.

The GPF modeling methodology requires only inputs from sensor sets commonly incorporated on production vehicles. Namely, the model utilizes: mass flow rate from the ECU, exhaust gas lambda post TWC, gas temperature entering the GPF (if a thermocouple is not available, TWC thermal models have been used in literature as virtual sensors for this input [16]) and GPF soot loading at time of tip out, for which high fidelity models or calibration tables have already been developed [16-18].

To develop and validate the spatially discretized GPF model the following methodology is adopted. First, the single zone model is adapted for the GPF of this study. Then the model parameters are identified for eight regeneration events and validated on five separate regeneration events for the new GPF. This demonstrates the universality of the lumped parameter single zone model. Then the lumped parameter model is adapted into a 3-zone finite volume model. This adaption includes changing boundary conditions and applying a set of modified equations to each zone. Each zone will use the prior zone's simulated temperature as a boundary condition, creating a cascading axial temperature profile. The multi-zone model is then trained and validated using the same experimental data sets as the single zone model. Finally, results from the single zone and spatially discretized models will be compared and discussed.

All the parameter identification discussed herein utilizes Particle Swarm Optimization, PSO, to optimize a Root Mean Square Error cost function, minimizing the difference between the simulated temperature profile and the experimental temperature profile. Particle Swarm Optimization is similar to genetic algorithms [20]. The PSO modulates various pre-exponential and exponential terms within the reduced order chemical reaction equations. These terms inherently affect the heat of reaction during regeneration, and therefore define the temperature profile during regeneration. The PSO optimizes the parameters to reduce the error between the simulated and experimental temperature profiles, for each zone.

Single Zone Model Formulation

Following the model development and assumptions provided by Arunachalam et al [18], the three major reaction pathways within a ceria coated GPF are laid out in equations 1-3. Rathod et al [19] experimentally found that CO concentrations were orders of magnitude less than CO_2, and Arunachalam et al [18] neglected CO oxidation in the model as a result.

$$C + O_2 \rightarrow CO_2 \tag{1}$$
$$C + 4CeO_2 \rightarrow 2Ce_2O_3 + CO_2 \tag{2}$$
$$Ce_2O_3 + 0.5O_2 \rightarrow 2CeO_2 \tag{3}$$
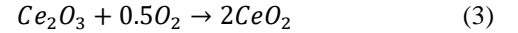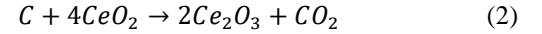
The Arrhenius equations for reaction rates are shown in Eq (4-6) where R_T is the reaction rate, A_t is the pre-exponential factor, R is the universal gas constant, T is the gas temperature, E_a is the reaction activation energy, m_c is the soot mass, M_c is the molar mass of Carbon, and X_{O2}, X_{CeO2} are the volume fraction of oxygen in the exhaust gas flow, and the volume fraction of free Ceria sites (available to react with carbon) respectively.

$$R_T = A_T \cdot e^{-\frac{E_a^T}{R \cdot T}} \cdot \frac{m_C}{M_C} \cdot X_{O_2} \tag{4}$$

$$R_{C,1} = A_{C,1} \cdot e^{-\frac{E_a^{C,1}}{R \cdot T}} \cdot \frac{m_C}{M_C} \cdot X_{CeO_2} \tag{5}$$

$$R_{C,2} = A_{C,2} \cdot e^{-\frac{E_a^{C,2}}{R \cdot T}} \cdot \frac{m_{O_2}}{M_{O_2}} \cdot (1 - X_{CeO_2}) \tag{6}$$

The Volume Fraction of active ceria sites is determined by:

$$\frac{dX_{CeO_2}}{dt} = -A_{C,1} \cdot e^{-\frac{E_a^{C,1}}{R \cdot T}} \cdot \frac{m_C}{m_C^0} \cdot X_{CeO_2} + A_{C,2} \\ \cdot e^{-\frac{E_a^{C,2}}{R \cdot T}} \cdot X_{O_2} \cdot (1 - X_{CeO_2}) \tag{7}$$

The carbonaceous soot mass is determined by:

$$\frac{dm_C}{dt} = -A_T \cdot e^{-\frac{E_a^T}{R \cdot T}} \cdot m_C \cdot X_{O_2} - A_{C,1} \cdot e^{-\frac{E_a^{C,1}}{R \cdot T}} \cdot m_C \\ \cdot X_{CeO_2} \tag{8}$$

The conservation of energy equation is the balance of convective heat transfer within the GPF and the heat of reactions during regeneration. $C_{p,g}$ is the specific heat of the gas, $\dot{m}_g$ is the mass flow rate of the exhaust gas, T_{in} is the inlet gas temperature, T_{sim} is the simulated GPF temperature, V_{cord} is the volume of cordierite substrate, ρ_{GPF} is the density of the cordierite, $C_{p,GPF}$ is the identified specific heat of the GPF, ΔH_x is the enthalpy of formation for each reaction, and R_x is the reaction rate.

$$\frac{dT}{dt} = \frac{\dot{m}_g \cdot C_{p,g} \cdot (T_{in} - T_{sim})}{V_{cord} \cdot \rho_{GPF} \cdot C_{p,GPF}}$$
$$+ \left(\frac{(-\Delta H_T)R_T + (-\Delta H_{C,1})R_{C,1} + (-\Delta H_{C,2})R_{C,2}}{V_{cord} \cdot \rho_{GPF} \cdot C_{p,GPF}} \right) \quad (9)$$
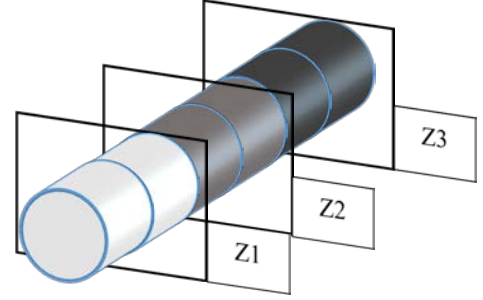
Table 4: Known Properties

ΔH_T	-393.5e3 $[J/mol]$
$\Delta H_{C,1}$	368.9e3 $[J/mol]$
$\Delta H_{C,2}$	-762.4e3 $[J/mol]$
E_a^T	149e3 $[J/mol]$
M_C	12e-3 $[kg/mol]$
M_{O_2}	32e-3 $[kg/mol]$

The enthalpies of formation, molecular weights and activation energy for the main CO_2 reaction are all fixed values, as shown in Table 4. Further information can be found about the development of these equations and determination of properties in Arunachalam et al. [18].

Spatial Discretization Methodology

To expand the fidelity of the model, the GPF is subdivided into three finite volume cells. Utilization of three modeling zones relates to the thermocouple locations during experimental testing, allowing a direct comparison of the model temperature prediction to the experimental measurements during identification and validation. Each volume is determined by placing the center line of the zone at the planar locations of the experimental thermocouples. Note that the three zones are not equal in volume due to the physical placement of experimental thermocouples. The volumes of Z1 and Z3 are equivalent while Z2 is one half the volume of zone 1 or zone 3. The boundary condition temperature within the conductive heat transfer term for each zone is a function of the previous zone, such that the model only needs to know the inlet gas temperature to predict all the zonal temperatures.

In addition, a new parameter was added to the identification set, the activation energy for Equation 4, E_a^T. Nicolin et al [17] noted that the temperature dependence of this activation energy and stated its range between 140,000 and 160,000 J/mol [17]. While a previous effort in catalytic GPF modeling chose to hold this term constant, the additional fidelity in reaction kinetics enabled by including this term in the model identification was found to improve model accuracy.

Figure 5: Spatial Representation of three Zones

The governing equations from the single zone model are adapted and implemented for each individual zone. The initial soot mass, as determined by the accumulation testing, is subdivided equally by volume into each zone due to the lack of experimental information on the spatial soot distribution. The model subdivision also dictates changes to the convective heat transfer term, where the temperature difference is now between the previous zone and the current zone, shown in the following equations as z(i) where i represents the 1st, 2nd, and 3rd zones, respectively. For the first zone, z(i-1) is the temperature of the exhaust gas at the inlet.

$$\frac{dm_{C(z(i))}}{dt} = -A_T \cdot e^{-\frac{E_a^T}{R \cdot T}} \cdot m_{C(z(i))} \cdot X_{O_2}$$
$$- A_{C,1} \cdot e^{-\frac{E_a^{C,1}}{R \cdot T}} \cdot m_{C(z(i))} \quad (9)$$
$$\cdot X_{CeO_2}$$

$$\frac{dX_{CeO_2}}{dt} = -A_{C,1} \cdot e^{-\frac{E_a^{C,1}}{R \cdot T}} \cdot \frac{m_{C(z(i))}}{m_C^0 * Frac_{z(i)}}$$
$$\cdot X_{CeO_2} + A_{C,2} \cdot e^{-\frac{E_a^{C,2}}{R \cdot T}} \cdot X_{O_2} \quad (10)$$
$$\cdot (1 - X_{CeO_2})$$

$$R_T = A_T \cdot e^{-\frac{E_a^T}{R \cdot T}} \cdot \frac{m_{C(z(i))}}{M_C} \cdot X_{O_2} \quad (11)$$

$$R_{C,1} = A_{C,1} \cdot e^{-\frac{E_a^{C,1}}{R \cdot T}} \cdot \frac{m_{C(z(i))}}{M_C} \cdot X_{CeO_2} \quad (12)$$

$$R_{C,2} = A_{C,2} \cdot e^{-\frac{E_a^{C,2}}{R \cdot T}} \cdot \frac{X_{O_2} \cdot \rho_{O_2} \cdot V_{trap\,z(i)}}{M_{O_2}} \quad (13)$$
$$\cdot (1 - X_{CeO_2})$$

$$\frac{dT_{(z(i))}}{dt} = \frac{\dot{m}_g \cdot C_{p,g} \cdot (T_{z(i-1)} - T_{zi})}{V_{cord(z(i))} \cdot \rho_{GPF} \cdot C_{p,GPF}}$$
$$+ \left(\frac{(-\Delta H_T)R_T + (-\Delta H_{C,1})R_{C,1} + (-\Delta H_{C,2})R_{C,2}}{V_{cord(z(i))} \cdot \rho_{GPF} \cdot C_{p,GPF}} \right) \quad (14)$$

Model Parameter Identification

Specific Heat Identification

The specific heat of the cordierite substrate within the GPF is required to develop the thermal GPF model. Thus, a clean (no soot accumulated) thermal sweep was conducted as per [19] to establish the thermal inertia of the GPF. The thermal sweep test subjects the GPF to a host of transients between real-world conditions while installed on the vehicle. The vehicle speed and load is ramped to an operating condition of interest, which is then held constant until the GPF temperatures stabilize. Subsequently, the vehicle is transiently ramped to another operating condition and the process repeats. The GPF specific heat was determined by running the PSO parameter identification for specific heat over the clean thermal sweep data, comparing the experimentally averaged temperature to the simulated temperature. Clean GPF operation allows the assumption that no heat is released from soot oxidation, therefore the GPF temperature is only a function of the steady state conservation of energy equation where the volume, mass flow rate, density, and gas specific heat were determined from experimentally measured values.

$$\frac{dT_{(sim)}}{dt} = \frac{\dot{m}_g \cdot C_{p,g} \cdot (T_{in} - T_{sim})}{V_{cord(z(i))} \cdot \rho_{GPF} \cdot C_{p,GPF}} \qquad (15)$$

The GPF was found to have a specific heat of 1136 [J/kg*K]. The PSO returned a simulated temperature profile with a RMSE of 0.16% relative to the experimental temperature profile. The specific heat of the GPF is similar to other specific heats of catalytically coated GPFs presented in literature [16, 18]. Figure 6 shows both the experimental temperature trace of the GPF, as well as the clean model prediction of GPF temperature.
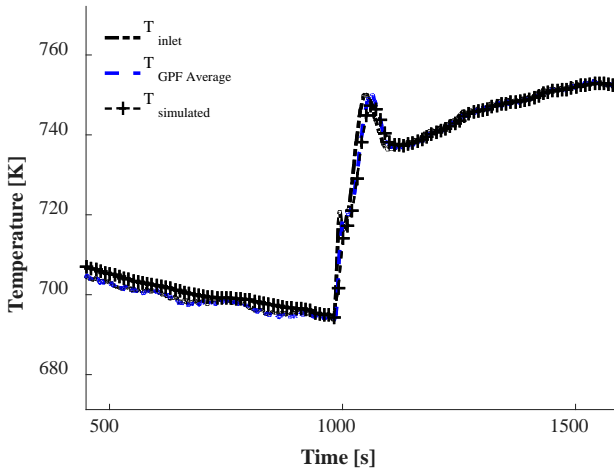

Figure 6: Specific Heat Parameter Identification.

Lumped Model

In this section, the model of Arunachalam et al [18] was reidentified for a second, physically different, GPF device. Owing to the thermal focus of this work, the cost function was modified to minimize the difference between the experimental averaged GPF temperature and the simulated temperature. A Particle Swarm Optimization algorithm [20] was used to optimize the five key parameters within the system of equations governing the temperature profile, shown in Table 5 for each of the regeneration and tip-out events. Due to the nature of the reduced order model, some of the parameters lose significant physical meaning to compensate for properties that were not accounted for in the model.

Equation (16), is presented in percentage, where T_{sim} is the modeled temperature, T_{exp} is the average of the three GPF centerline thermocouples, and n is the time step index.

$$RMSE = \sqrt{\frac{1}{n} * \sum_{i=1}^{n} \left(\frac{T_{sim(i)} - T_{exp}}{\max(T_{exp})} \right)^2} * 100 \qquad (16)$$

$$\theta = \begin{bmatrix} E_a^{C,1} & E_a^{C,2} & A_T & A_{C,1} & A_{C,2} & E_t \end{bmatrix} \qquad (17)$$

Table 5: Parameter Identification Range

Parameter	Identification Range	Units
$E_a^{C,1}$	[1E3, 1E7]	[J/mol]
$E_a^{C,2}$	[1E3, 1E7]	[J/mol]
A_T	[1, 1E9]	[1/s]
$A_{C,1}$	[1, 1E7]	[1/s]
$A_{C,2}$	[1, 1E7]	[1/s]
E_a^T	[140E3, 160E3]	[J/mol]

The cost function and parameter identification range for the PSO are included in Eq (17) and Table 5, respectively. However, for the lumped model, the activation energy E_a^T was reduced to a constant (noted in Table 4), and not modulated by the PSO, as to provide a direct comparison of the model developed in Arunachalam et al [18].
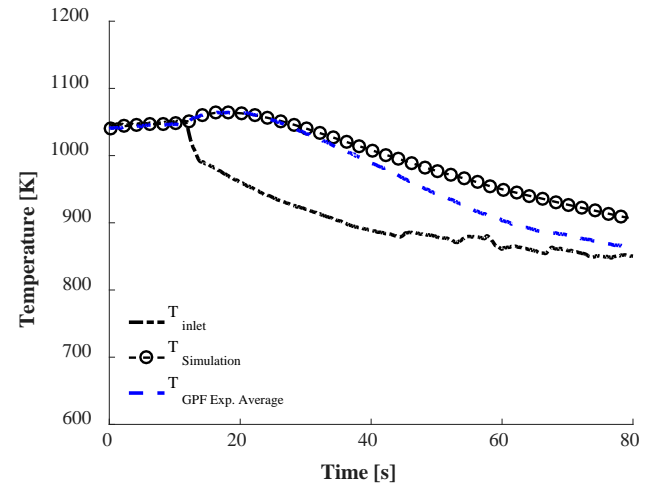

Figure 7: Regeneration 2C Single Zone Identification Set

The change in slope between simulation and experimental data after the regeneration event in Figure 7 and subsequent temperature profiles is postulated to be a function of the

identified specific heat of the GPF. The specific heat was determined under conditions of relatively high mass flow and high exhaust temperatures at the GPF inlet. The testing portion directly after regeneration (beginning just before 40s in Figure 7) is characterized by lower mass flow rate (5x less) and atmospheric oxygen flow, as seen in Figure 3, which results in low GPF inlet temperatures. Furthermore, the model does not incorporate external convective heat loss, which becomes much larger in relation to overall heat transfer after regeneration both because of the relatively low mass flow rate and the higher GPF temperatures. This work focuses on modeling regeneration and peak temperatures as accurately as possible, as such the deviation was left for future work.

Spatially Discretized GPF Model Identification

The spatially discretized model PSO identification included another parameter, E_a^T, the activation energy for the carbon oxidation reaction. Inclusion of this additional identified parameter allowed the PSO to more rapidly and accurately optimize all other parameters. Owing to the model's high degree of sensitivity to the carbon reaction activation energy, the term was bounded carefully around values found in literature (140,000 – 160,000 j/mol) [17]. The identification ranges for all identified parameters are shown in Table 5. For brevity, the identified parameter values for both the 0D model and each zone of the spatially discretized model are displayed in the appendix. Figures 8 and 9 are comparison plots of model predicted temperature and experimental temperature traces for two of the eight identification sets. The authors note that, to improve model performance and assist in removing complications from the tail end discrepancy noted in the section prior, the RMSE values and PSO optimization 'range' was selected to operate between tipout and 20 seconds after peak temperature in zone 3, the zone with the highest temperature in all sets. This 'range' is depicted as the green vertical bars in Figure 8.
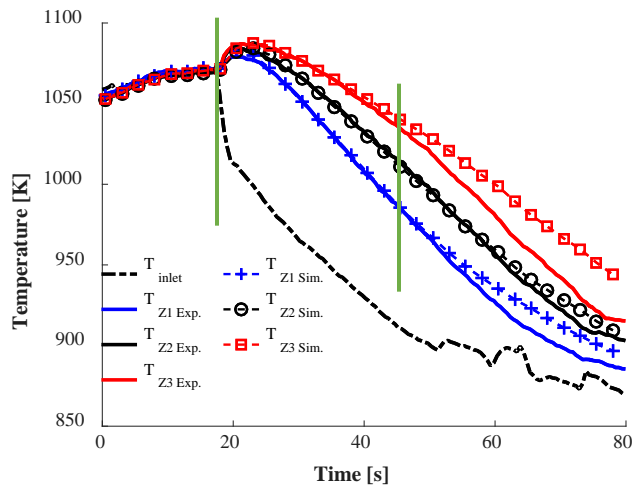

Figure 8: Identification Set 1B – 1050K @ Tip-out, 0.3 g soot oxidized. Experimental temperature traces are denoted "Z(i) Exp" while the simulated temperatures are denoted "Z(i) Sim"
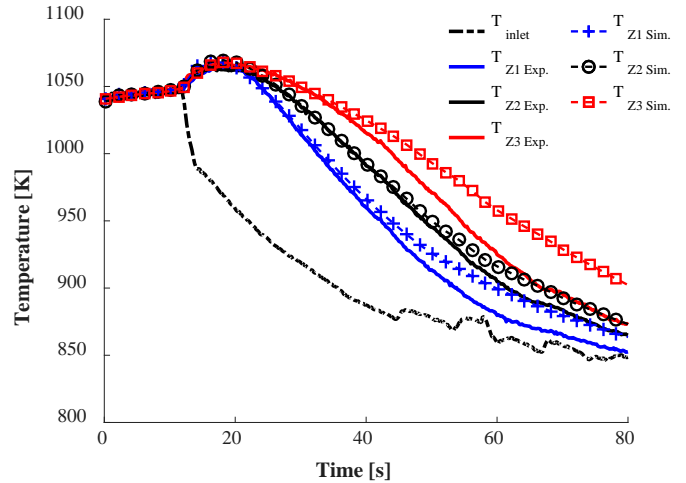

Figure 9: Identification Set 2C -1050K Tip-out Temperature, 0.32 g soot oxidized.

Identification Result Comparison

The identification RMSE values for both the lumped and the three Zone GPF models are shown in Table 6. The RMSE is calculated individually for each zone in the three zone model using the same cost function as the lumped model, where T_{avg} is replaced with $T_{Z(i),Exp}$, the temperature of the zone being identified. The RSME performance of the individual spatial zones is very similar to the RSME of the lumped model. For all eight identification regeneration events, the worst performing RMSE value for the lumped model was 1.04 %, and the best was 0.12 %, for the Three Zone model the values were 0.72 % and 0.09 %, respectively.

Table 6: RMSE Lumped and Three Zone Comparison

	Lumped	Three Zone		
	[%]	Zone 1 [%]	Zone 2 [%]	Zone 3 [%]
1A	0.85	0.55	0.19	0.57
1B	0.12	0.19	0.18	0.09
1C	0.39	0.23	0.13	0.72
2A	1.59	0.57	0.31	0.47
2B	0.85	0.10	0.12	0.12
2C	0.71	0.35	0.31	0.12
2D	0.65	0.20	0.18	0.17
2E	1.04	0.58	0.36	0.41

Creation of a Linear Parameter Varying Model

To best implement a dynamic temperature model online, the model must account for all soot loading and tip-out temperature combinations, as both strongly affect regeneration. A linear parameter varying model was developed utilizing the identified

parameter values within a lookup table, such that, for any given GPF soot loading and the inlet temperature, the model can find the closest identified parameter values. The model then interpolates between the closest parameter values and predicts the internal GPF temperature using the same equations as the identification model. Given a GPF inlet temperature and soot loading, the 0D LPV is characterized by five parameters and predicts the average GPF temperature. In the case of the spatially discretized model, given inlet gas temperature and soot loading, the LPV determines 18 parameters, six per zone, and predicts three zonal temperatures. The additional parameter for the zonal model is the activation energy for the carbon oxidation reaction.

The authors note that due to the limited range of soot loading amongst the identification data sets, the model shows a lack of sensitivity to soot loading in comparison to GPF temperature at tip-out. The soot loading for the 1.8 SLD validation regeneration events is far closer to the 1.92 SLD identification than the 0.79 identification events, and, as such, the interpolation was heavily skewed towards the 1.92 SLD set. The model was developed to predict temperature profiles, so only the tip-out temperature interpolation aspect of the model was utilized based on the 1.92 SLD set. Identification for many initial soot loadings is needed for complete characterization of soot loading effect on parameter identification.

Model Validation

The three zone and lumped GPF models are compared using two metrics: (i) The PSO cost function determines the overall RMSE between the simulated and experimental temperatures (Zonal or Average). (ii) The absolute error in maximum GPF temperature relative to the model's predicted maximum temperature is tracked to gauge the potential utilization of each model for GPF health monitoring.

Lumped GPF Model Validation

The 0D model was applied to five regeneration sets, 3A-3E, see Table 7. Figure 10 depicts a representative regeneration event, 3B, which had an RMSE of 0.55% and a differential in maximum predicted temperature of 10K.
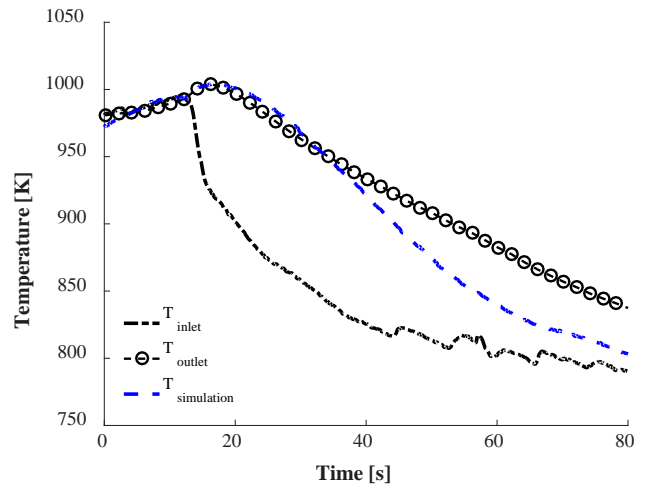

Figure 10: Regeneration 3B Validation Set - Single Zone

Three Zone GPF Model Validation

The three zone Linear Parameter Varying model was applied to the same five validation sets as the lumped LPV model. The worst performing validation set had an RMSE of 2.09 %, and the best performing had an RMSE of 0.30 %. A representative validation case, 3C, is presented in Figure 11. This validation data set produced an RMSE of 1.86, 1.36, and 0.53% for zones 1, 2, and 3, respectively. The third zone's maximum simulated temperature differed from the experimentally determined GPF peak temperature by only 2.7K.
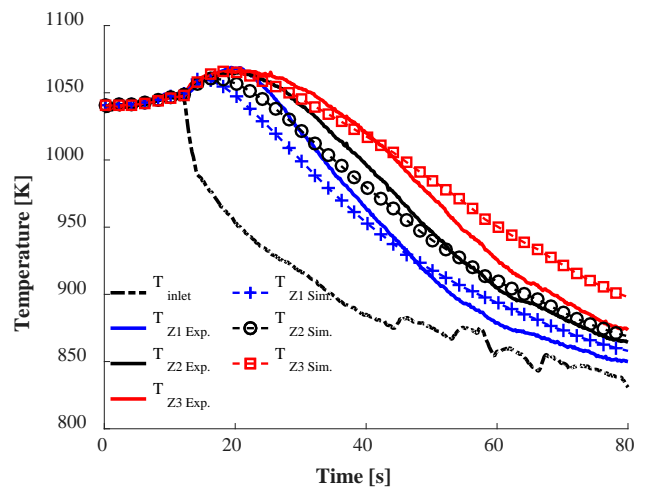

Figure 11: Three Zone Model Validation – data set 3C

Detailed Model Comparison – Lumped to Spatial

The lumped and three zone models are directly compared in Figure 12. For this case, the single zone model deviates in maximum predicted temperature by 10.1K at the peak location, while the three zone model is within 0.87K of the experimental peak temperature.

Figure 12: Comparison of Single and Multizone Models – data set 3B

Table 7: LPV Validation – RMSE Comparison

	Lumped	Three Zone		
	[%]	Zone 1 [%]	Zone 2 [%]	Zone 3 [%]
3A	2.95	2.09	1.84	1.59
3B	0.55	0.96	0.51	0.30
3C	2.14	1.86	1.36	0.53
3D	0.54	1.98	1.46	0.38
3E	1.48	1.30	1.18	0.50

Table 8: LPV Validation - Maximum Temperature Error Comparison

	Lumped	Three Zone		
	ΔT [K]	Z1 ΔT [K]	Z2 ΔT [K]	Z3 ΔT [K]
3A	44	15.9	21.5	20.1
3B	10	0.75	1.1	0.87
3C	32	19.1	10.2	2.71
3D	11	2.2	0.41	0.81
3E	28	4.8	12.2	0.29

Tables 7 and 8 provide detailed comparisons of the RSME values and error in maximum GPF temperature prediction for all the validation data. The three zone model improves upon the peak GPF temperature prediction for every validation data set, highlighting the improved accuracy via spatial discretization. From a health monitoring perspective, zone three has the highest temperature, and therefore is the most critical, and limiting temperature. Not only does the spatially discretized three zone model improve upon modeling accuracy over the entire regeneration event, shown by decreased RMSE values, the model improves peak temperature prediction 2-10X.

Discussion

The thrust of this work was to develop a model that more accurately depicted the spatial variation in temperature within a catalytically coated GPF. In order to maintain the health of a GPF over the life of a vehicle, it is critical to predict and intercede with any regeneration event that may generate exotherms beyond the GPF material limits. The highest temperatures within the GPF are always found during regeneration events in Zone 3, the most downstream experimental measurement location within the GPF. In Figure 12, the single zone, three zone, and experimental temperatures are plotted. When comparing the disparities between predicted maximum temperature and the measured maximum GPF temperature, the 3-zone model outperforms the single zone model. For GPF health monitoring the 3-zone model provides the necessary fidelity to predict an exotherm that will exceed the maximum allowable temperature and intervene accordingly. As mentioned in Arunachalam et al [18] and Rathod et al [19], successive fuel-cut tip-out regeneration events at higher temperatures were needed as the GPF rapidly cooled during tip-out, dropping temperatures below the catalyst light off temperature. The LPV model can be incorporated within a DFSO control strategy to alter the coast down event and maintain higher GPF temperatures when additional soot oxidation is desired.

Conclusions

Thermal mechanical GPF degradation and component failure from exceeding temperature limits of either the GPF substrate or the catalyzed washcoat is a critical concern for the control and management of a GPF over its useful life. This work presents a reduced order thermal model for thermal protection control strategies for GPF health monitoring. To summarize:

- The 0D lumped parameter model was shown to be applicable to GPF designs of varying geometry and material properties.
- A spatially discretized, control oriented thermal model was parametrized, identified, and validated over 13 regeneration events.
- Spatial discretization improves the GPF model's peak temperature predictions to within a 3K of the experimental measurements for 4 out of 5 validation regeneration events.
- Spatial discretization decreased maximum predicted temperature error 2-10x relative to the lumped GPF model.
- Three Zone Model requires only inputs that are already available on production vehicles. No additional sensors are required.

Future Work

Sources [11] have shown experimentally that soot oxidation is not equally dispersed within GPFs. Further work is required to modify the LPV model to quantify the zonal distribution of soot.
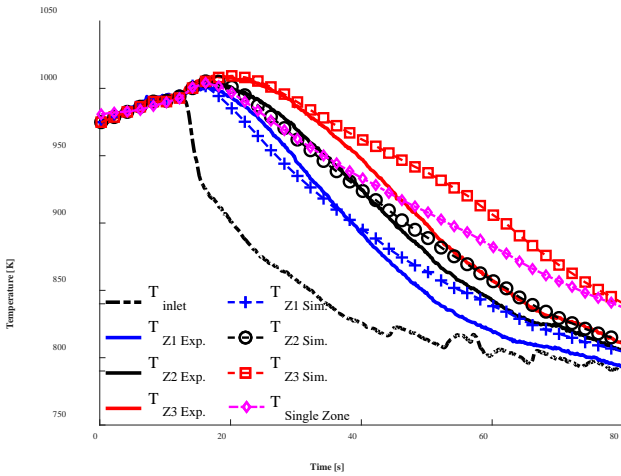
NOMENCLATURE

A_t, $A_{c,1}$, $A_{c,2}$ = Pre-exponential factor for Arrhenius Reaction Rate Equations
$C_{p,g}$ = Specific Heat, Exhaust Gas
$C_{p,GPF}$ GPF Specific Heat
DFSO = Deceleration Fuel Shut Off
DMS = Differential Mass Spectrometer
DPF = Diesel Particulate Filter
E_a = Activation Energy
ECU = Engine Control Unit
FTIR = Fourier Transform Infrared Spectroscopy
FTP75 / USO6 = Federal Test Procedure 75, Supplemental Federal Test Procedure (USO6)
GPF = Gasoline Particulate Filter
GDI = Gasoline Direct Injection
LPV = Linear Parameter Varying Model
Lumped Model = 'Single Zone', 0D Model
MAP = Manifold Absolute Pressure
$\dot{m}_g$ = Mass Flow Rate, exhaust gas
M_c = Molar Mass, Carbon
m_c = mass of soot accumulated within GPF
M_{O2} = Molar Mass, Oxygen
NEDC = New European Drive Cycle
PFI = Port Fuel Injection
PM/PN = Particulate Matter, Particulate Number
PSO = Particle Swarm Optimization
ρ_{GPF} = Density of Cordierite Substrate, GPF
R = Universal Gas Constant
RMSE = Root Mean Square Error
SLD = Soot Loading Density
T_{sim} = Model Generated, Simulated Temperature
TWC = Three Way Catalyst
V_{Cord} = Volume of Cordierite substrate in GPF
WLTC = Worldwide Harmonized Light Vehicle Test Procedure
X_{o2} = Volume fraction, Oxygen or Ceria

REFERENCES
1. Chan, T., Meloche, E., Kubsh, J., Rosenblatt, D. et al., "Evaluation of a Gasoline Particulate Filter to Reduce Particle Emissions from a Gasoline Direct Injection Vehicle," SAE Int. J. Fuels Lubr. 5(3):1277-1290, 2012
2. Shimoda, T., Ito, Y., Saito, C., Nakatani, T. et al., "Potential of a Low Pressure Drop Filter Concept for Direct Injection Gasoline Engines to Reduce Particulate Number Emission," SAE Technical Paper 2012-01-1241, 2012
3. Kern, B., Spiess, S., and Richter, J., "Comprehensive Gasoline Exhaust Gas Aftertreatment, an Effective Measure to Minimize the Contribution of Modern Direct Injection Engines to Fine Dust and Soot Emissions?," SAE Technical Paper 2014-01-1513, 2014
4. Demuynck, J., Favre, C., Bosteels, D., Hamje, H. et al., "Real-World Emissions Measurements of a Gasoline Direct Injection Vehicle without and with a Gasoline Particulate Filter," SAE Technical Paper 2017-01-0985, 2017
5. Czerwinski, J., Comte, P., Heeb, N., Mayer, A. et al., "Nanoparticle Emissions of DI Gasoline Cars with/without GPF," SAE Technical Paper 2017-01-1004, 2017
6. Ogata, T., Makino, M., Aoki, T., Shimoda, T. et al., "Particle Number Emission Reduction for GDI Engines with Gasoline Particulate Filters," SAE Technical Paper 2017-01-2378, 2017.
7. Chan, T., Meloc he, E., Kubsh, J., Brezny, R. et al., "Impact of Ambient Temperature on Gaseous and Particle Emissions from a Direct Injection Gasoline Vehicle and its Implications on Particle Filtration," SAE Int. J. Fuels Lubr. 6(2):350-371, 2013
8. Richter, J., Klingmann, R., Spiess, S., and Wong, K., "Application of Catalyzed Gasoline Particulate Filters to GDI Vehicles," SAE Int. J. Engines 5(3):1361-1370, 2012
9. Xia, W., Zheng, Y., He, X., Yang, D. et al., "Catalyzed Gasoline Particulate Filter (GPF) Performance: Effect of Driving Cycle, Fuel, Catalyst Coating," SAE Technical Paper 2017-01-2366, 2017.
10. Locker, Robert J., N. Gunasekaran, and Constance Sawyer. "Diesel Particulate Filter Test Methods." SAE Technical Paper Series, 2002. doi:10.4271/2002-01-1009.
11. Sappok, A., Wang, Y., Wang, R., Kamp, C. et al., "Theoretical and Experimental Analysis of Ash Accumulation and Mobility in Ceramic Exhaust Particulate Filters and Potential for Improved Ash Management," SAE Int. J. Fuels Lubr. 7(2):511-524, 2014
12. Lambert, C., Bumbaroska, M., Dobson, D., Hangas, J. et al., "Analysis of High Mileage Gasoline Exhaust Particle Filters," SAE Int. J. Engines 9(2):1296-1304, 2016
13. Bernardoff, R., Hennebert, B., Delvigne, T., Courtois, O. et al., "A Study of Ash Accumulation in the After-treatment System of a Gasoline Direct Injection Engine Equipped with a Gasoline Particulate Filter," SAE Technical Paper 2017-01-0879, 2017
14. Rubino, L., Thier, D., Schumann, T., Guettler, S. et al., "Fundamental Study of GPF Performance on Soot and Ash Accumulation over Artemis Urban and Motorway Cycles - Comparison of Engine Bench Results with GPF Durability Study on Road," SAE Technical Paper 2017-24-0127, 2017.
15. Lambert, C., Chanko, T., Jagner, M., Hangas, J. et al., "Analysis of Ash in Low Mileage, Rapid Aged, and High Mileage Gasoline Exhaust Particle Filters," SAE Int. J. Engines 10(4):1595-1603, 2017
16. Van Nieuwstadt, M. and Ulrey, J., "Control Strategies for Gasoline Particulate Filters," SAE Technical Paper 2017-01-0931, 2017.
17. Nicolin, P., Rose, D., Kunath, F., and Boger, T. 2015. Modeling of the Soot Oxidation in Gasoline Particulate Filters. SAE International Journal of Engines 8, 2015-01–1048.
18. Arunachalam, H. Pozzato, G. Hoffman, M. Onori, S. "Modeling the thermal dynamics inside a ceria-coated Gasoline Particulate Filter." In *Control Technology and Applications (CCTA), 2017 IEEE Conference on*, pp. 99-105. IEEE, 2017.
19. Rathod, D. Hoffman, M. Onori, S. Filipi, Z. "Experimental Investigation Of Soot Accumulation And Regeneration In A

Catalyzed Gasoline Particulate Filter Utilizing Particulate Quantification And Gas Speciation Measurements." *ASME International Combustion Engine Fall Technical Conference"* ASME-2018-9627. San Diego, CA.

20. Ebbesen, S., Kiwitz, P., & Guzzella, L. (2012). A generic particle swarm optimization Matlab function. *American Control Conference (ACC), 2012*, 1519–1524. https://doi.org/10.1109/ACC.2012.6314697

Appendix

Table 9: Single Zone Parameter Identification Values

#	$E_a^{C,1}$	$E_a^{C,2}$	A_T	$A_{C,1}$	$A_{C,2}$
1A	693222.7	114061.5	989796.2	100.0	365467.2
1B	162497.4	109431.6	99.9	196069.0	159459.8
1C	122954.1	112148.4	100.0	63263.4	167953.0
2A	117229.0	123173.6	6215050.0	118062.6	207813.2
2B	115012.2	101138.4	4564028.0	71836.9	20960.7
2C	115337.6	122686.6	4325779.0	239220.2	92453.8
2D	117273.2	100984.1	1296489.0	58674.2	25765.5
2E	20160.7	116780.5	5302609.0	100.0	79610.9

Table 10: Multi-zone Parameter Identification Values for Zone 1

#	$E_a^{C,1}$	$E_a^{C,2}$	A_T	$A_{C,1}$	$A_{C,2}$	E_t
1A	833000000.0	1000000000.0	24442830.0	955000000.0	311000000.0	160000.0
1B	2017241.0	51737.1	1805653.0	1526440.0	100.0	140020.1
1C	500735.3	139541.2	1337770.0	100.0	1346996.0	140022.3
2A	8996566.0	4602905.0	38268828.0	9195385.0	3099374.0	160000.0
2B	5166375.0	9948174.0	41489201.0	528705.7	5393439.0	160000.0
2C	4813640.0	145010.0	11118095.0	396362.2	4101924.0	154847.9
2D	365781.8	6857298.0	11914909.0	1759903.0	4926238.0	160000.0
2E	198361.4	121740.7	1443143.0	249410.3	189558.2	140446.3

Table 11: Multi-zone Parameter Identification Values for Zone 2

#	$E_a^{C,1}$	$E_a^{C,2}$	A_T	$A_{C,1}$	$A_{C,2}$	E_t
1A	142572.0	106345.4	100.0	22043.9	172604.0	140000.3
1B	107101.7	73180.3	144.3	9575.8	2686.6	140007.2
1C	111363.3	131573.2	100.0	143564.8	143670.7	140405.6
2A	55135.8	21717.6	2237644.0	8272.1	1.0	140053.5
2B	58885.7	61437.7	3080281.0	1256.8	234.2	140000.0
2C	87868.5	90000.8	18188629.0	71215.0	188400.5	140331.0
2D	74703.2	105762.9	1.0	289.7	106945.5	140000.0
2E	4323158.0	9999998.0	642000000.0	4451393.0	7103092.0	160000.0

Table 12: Multi-zone Parameter Identification Values for Zone 3

#	$E_a^{C,1}$	$E_a^{C,2}$	A_T	$A_{C,1}$	$A_{C,2}$	E_t
1A	142572.0	106345.4	100.0	22043.9	172604.0	140000.3
1B	107101.7	73180.3	144.3	9575.8	2686.6	140007.2
1C	111363.3	131573.2	100.0	143564.8	143670.7	140405.6
2A	55135.8	21717.6	2237644.0	8272.1	1.0	140053.5
2B	58885.7	61437.7	3080281.0	1256.8	234.2	140000.0
2C	87868.5	90000.8	18188629.0	71215.0	188400.5	140331.0
2D	74703.2	105762.9	1.0	289.7	106945.5	140000.0
2E	4323158.0	9999998.0	642000000.0	4451393.0	7103092.0	160000.0